APPLICATION OF ELECTROMAGNETIC-BANDGAP STRUCTURES
TO POWER DISTRIBUTION NETWORK DESIGN

BY

YIXUAN NANCY ZHAO

THESIS

Submitted in partial fulfillment of the requirements
for the degree of Master of Science in Electrical and Computer Engineering
in the Graduate College of the
University of Illinois at Urbana-Champaign, 2019

Urbana, Illinois

Adviser:

Professor José Schutt-Ainé

ABSTRACT

This thesis provides a detailed literature review and an original pattern design example of the application of an electromagnetic bandgap structure which suppresses the simultaneous switching noise in a power distribution network. By accommodating a metalized periodic pattern on either power or ground plane, the performance of multilayer digital circuit boards can be enhanced with minimized electromagnetic interference. Both numerical and analytical validation are demonstrated to show the effectiveness of the new pattern implementation.

To my parents and friends, for their love and support.

ACKNOWLEDGMENTS

I would like to acknowledge the individuals whose support and mentorship made it possible for me to arrive at this stage of life. Foremost, I thank Professor José Schutt-Ainé for welcoming me into his research group, guiding me to accomplish both my bachelor's and master's theses, and being an incredibly patient advisor.

Next, to all my colleagues and friends, I would never have completed this thesis without your help. In particular, I would like to thank my colleague Thong Nguyen, who always complimented and credited me for every small step of success; Xu Chen, who gave me directions and mentored me since my undergraduate years; Xiao Ma, who provided me an unlimited gum supply and rode the same thesis-writing-struggle-bus together with me and last but not least, Bobi Shi, who delivered countless takeouts to me when I had to study late at night. In addition, I thank my friend Siyan Guo, who chose to be my roommate for five years yet still does not hate me, and Jingchao Zhou and Qing Ding, who spent hundreds of their valuable hours video-gaming with me and saved me from depression. My list of all the nice people I met in my seven years of corn-field life could go on and on. Wholeheartedly, I wish them the brightest future, either in academia or industry.

Finally, I would like to thank my mom and dad. It must have been a tough decision for them to wave goodbye to me, sending me to complete my education in a country ten thousand miles from home. I am so honored to be where I am now. Love. NZ.

TABLE OF CONTENTS

LIST OF FIGURES

LIST OF ABBREVIATIONS

EBG   Electromagnetic Bandgap.

EMI   Electromagnetic Interference.

FEM   Finite Element Method.

GBN   Ground Bounce Noise.

HIS   High-Impedance Surface.

NRZ   Non-Return to Zero.

PCB   Printed Circuit Broad.

PDN   Power Distribution Network.

PI   Power Integrity.

PPW   Parallel Plate Waveguide.

PRBS   Pseudo-Random Binary Sequence.

RF   Radio Frequency.

SI   Signal Integrity.

SSN   Simultaneous Switching Noise.

TE   Transverse Electric.

TM   Transverse Magnetic.

CHAPTER 1

INTRODUCTION

1.1 Motivation

With an increasing demand for low-cost, reduced-size and high-speed compact IC design, degradation of the signal integrity (SI) due to the fast-transient current has become a major concern. Conventionally, designated discrete capacitors from the power distribution network (PDN) are sufficient to prevent momentary fluctuations of ground voltage within the device even when multiple signals switch simultaneously. However, where high-frequency clock signal is present, the use of a decoupling capacitor will induce ground bouncing noise (GBN) and simultaneous switching noise (SSN) because of the lead parasitic inductance. At PCB or package level, this noise will propagate through the parallel plate waveguide (PPW) formed by the power and ground planes, introducing electromagnetic interference (EMI) issues into the PDN. More specifically, jitter or noise spikes within the same PDN interconnect will affect the return current of the signal lines that pass the peripheral via holes. Thus, the immediate consequence of this cavity resonance includes not only excessive noise on the voltage rails of the chips, but also deterioration of the performance of extremely sensitive RF/analog circuits. Many researches have been conducted to resolve the propagation of SSN, including the proper selection of via location to suppress certain package resonance [1], application of differential interconnect design that rejects the common mode noise [2], and usage of buried decoupling capacitors [3]. Nevertheless, these methods all focus on the localized suppression of SSN, which can be highly design-specific. In order to obtain a global solution that has excellent SSN isolation throughout the required bandwidth (100 MHz to 20 GHz), periodic electromagnetic bandgap structure (EBG) is nominated for its special characteristic of rejecting certain frequency bands of electromagnetic waves at all angles

and all polarization states [4]. EBG structure is commonly used in antenna substrates for surface wave suppression. It enhances the antenna's efficiency and gain by directing the EM waves to radiate in the main beam direction instead of propagating along the ground plane. Furthermore, EBG structure also provides a high-impedance surface (HIS) due to its semi-discrete metal patches [5]. HIS supports TM mode waves only at lower frequency and TE mode waves only at higher frequency. By designing the forbidden bandgap of EBG to match the resonant mode frequencies of the rectangular cavity, the power/ground plane pair will effectively behave as a perfect magnetic conductor that allows neither TE nor TM mode waves to exist.

1.2 Outline

This thesis is organized into five chapters.

Chapter 1 introduces the background and basic properties of EBG structures. The motivation of integrating EBG to PDN design is also explained.

Chapter 2 gives a detailed literature review on the history of how the EBG structure evolved in antenna engineering over the years and eventually found use in PDN design. The reviewed papers were classified into four main categories based on the proposed structure's fabrication cost (given that more complex geometry often results in lower yield).

Chapter 3 discusses the proper design process flow for EBG patterns to achieve the desired electrical characteristics. Parametric study on a sample EBG structure is performed first, followed by transforming the pattern's geometric parameters into equivalent filter circuit.

Chapter 4 presents the design flow of an optimized low-period EBG pattern which demonstrated board-band SSN suppression. After forming the prediction band with the equivalent filter circuit, an optimization code is used to generate the input parameters to feed into the finite element solver.

Chapter 5 draws conclusions and discusses the possibility of further optimizing the EBG pattern design flow.

CHAPTER 2

LITERATURE REVIEW

2.1 EBG Theory

The concept of EBG was first introduced in solid-state physics and optics in 1987 [6]. Although it had a slightly different design focus than the subject of this thesis, it is important to answer why and how this structure was invented to fully understand the terminology. Without delving too much into the photonic crystal level of the structure, the physics behind the band-gap formation in EBG can be simplified to macroscopic and microscopic resonance of a periodic structure [7]. It is found that the periodicity mainly contributes to the macroscopic resonance (Bragg resonance) which, when cascaded, inhibits waves for all incident angles [8]. The microscopic resonance, which is also called Mie resonance [9], is due to the metamaterial's crystal alignment. Since the resonance frequency band can be intentionally designed to reject all incident waves, it provides a novel solution for applications that require certain stop-bands.

2.2 EBG Structure in Antenna Application

Besides optics, antennas are one of the first few areas where EBG structure has thrived. The design philosophy is illustrated in Figure 2.1. For the classical design on the left, the $\lambda/4$ gap between the radiation plane and ground redirects the reflected wave so it creates a constructive interference with the radiating wave. Nevertheless, as the design size becomes more compact, it is desirable to shrink the gap between the planes as much as possible. With the EBG structure on the right, it is possible to design the gap to be one eighth that of the classic one because the wave radiation has
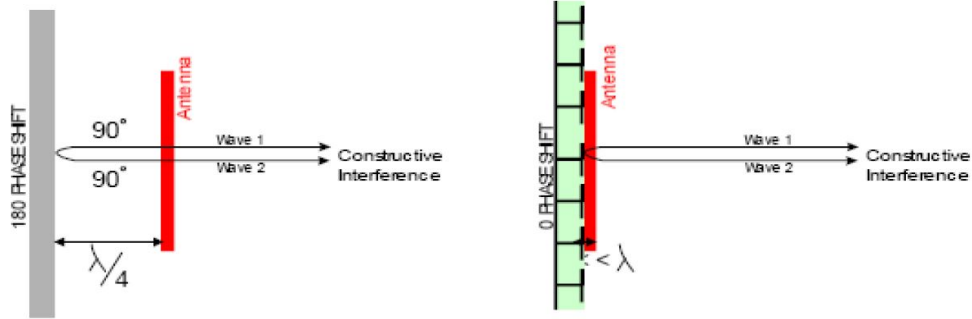
Figure 2.1: An antenna separated by $\lambda/4$ from the ground plane (on the left) and its EBG structure alternative (on the right) [7].
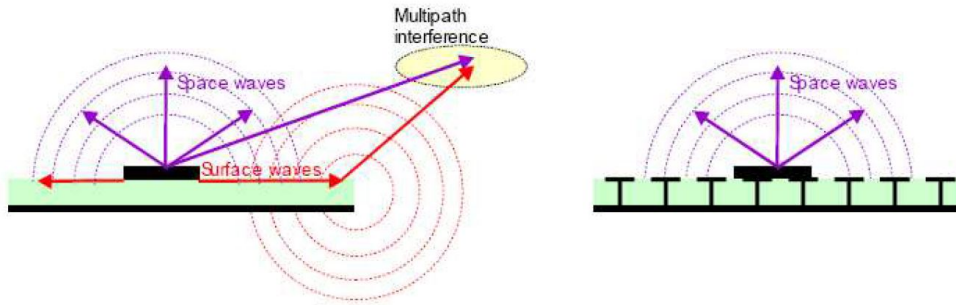
Figure 2.2: Multipath interference due to surface waves on the ground plane (on the left) and its EBG alternative (on the right) [7].

relatively weak coupling with gap width. In addition, the classic design is not so effective in suppressing the undesired propagation of the surface wave on the ground plane due to its planar structure. As shown in Figure 2.2, the surface wave could be significant and radiates as another small antenna which interferes with the original radiation path. This issue is solved in the EBG structure because the surface impedance dramatically increases due to the uneven radiation plane design. Therefore, the EBG structure has many promising applications such as high-precision GPS, mobile devices and medical detectors.

2.3   EBG Structure in PDN Application

As briefly discussed in the introduction, PDN interconnects nowadays suffer from SSN and GBN because of the high-frequency clock requirement. For the readers who are not familiar with PDN design, it has to be emphasised

why this issue can be severely detrimental. As a key component of any electrical system that requires power delivery, the PDN's first priority is to keep a constant and stable supply voltage to all modules on the package level. Especially in a commercial board where ten or more layers of PCB are adopted, the PDN must provide a continuous and low-impedance current return path for the signal lines too. This means that PDN interconnects are usually the largest conducting plane present in the board, where the highest current and noise oftentimes overlap each other. Improper design could potentially introduce excessive noise that goes beyond the safe margin for the chips to correctly decode the bit or the clock. If bit failure and timing errors occur, it would take a whole design cycle to fix the problem because the noise specifications of all the modules need to be redefined. Thus, to mitigate the noise radiating in the the cavity of PDN, the EBG structure is integrated to the power/ground plane such that its forbidden band is carefully selected to overlap the PDN's noise band.

Four main categories of design topology were suggested in the past literature. The differentiation is made based on their structure rather than geometry. While all the aforementioned works share the common merit of utilizing HIS to create a proper band stop filter at the clock's first harmonic frequency, their performance varies depending on the implementation. The subsections below provide a detailed summary of each method's advantages and drawbacks.

2.3.1 Periodic Surface Patch

Given that the traditional decoupling capacitors between the PPW do not yield enough suppression of SSN beyond 500 MHz, Kamgaing and Ramahi introduced a novel technique that replaces the power ground pair with HIS [10]. As shown in Figure 2.3, the model is constructed by adding a periodic hexagon-shaped patch connected to the solid ground plane with two vias, thereby forming a high-pass filter with cut-off frequency at 4 GHz. Note that due to the small physical dimension of the structure, the HIS used here is a modified version of the EBG structure developed by Archambeault and Ruehli [11], which has its resonant frequency between 5 and 10 GHz. Since HIS can be modeled as a parallel LC resonant circuit [5], using a double
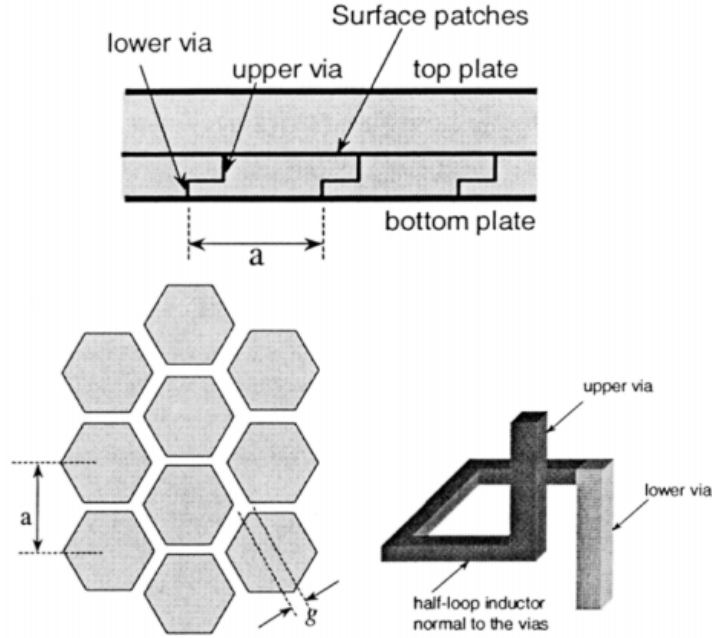
Figure 2.3: Typical example of periodic EBG surface patch [10].

layer of patches increases the fringing capacitance and therefore lowers the
center frequency. Meanwhile, straight metallic vias were replaced by half-
loop vias. This arrangement ensures a greater bandwidth without increasing
the thickness or cost of the dielectric substrate. The result shows good noise
suppression of S_{21} below -20 dB from 1 GHz to 3.3 GHz. A similar structure
was studied in [12] with more information in the time domain. Based on
their TDR measurement, the PPW noise peak is reduced by half if an EBG
patch is used with proper edge termination at the PCB sidewalls. If more
suppression is needed, one can also replace the FR4 between the patch and
plane with high dielectric constant thin film [13]. Further study of this patch
structure was carried out by Chen et al. emphasizing the effect of patch cell
geometry and alignment [14]. According to their observation, one can tune
the patch's size, gap width and shape to influence its corresponding filter
behavior. However, no exact formula was provided in the paper to explicitly
explain the mathematical relation of the factors mentioned.

(a) 3-D view and the locations of three ports. **(b)** Parameters of a square unit cell.
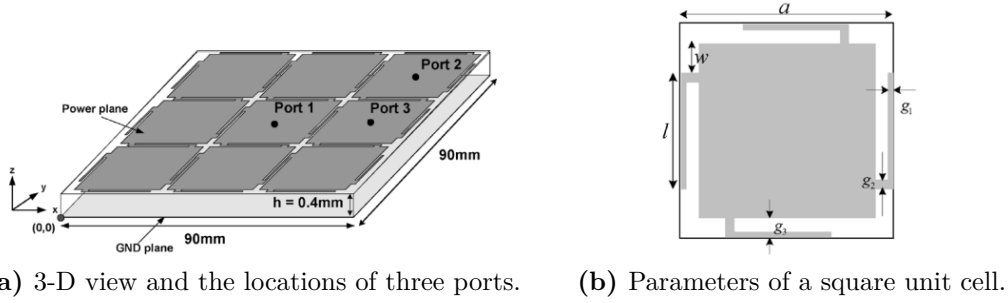
Figure 2.4: Nine-cell co-planar EBG structure with L-Bridge [15].
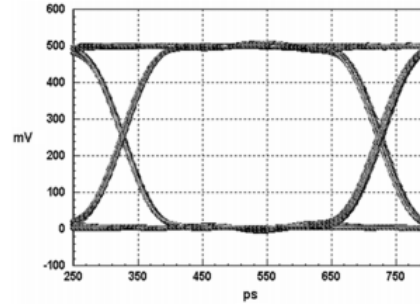
2.3.2 Patterned Power Plane

Without the effort of drilling vias or attaching additional patches, Wu et al. designed a novel co-planar EBG structure that works with 4 GHz stop-band covering from 600 MHz to 4.6 GHz [15]. The periodic pattern is etched on the power plane and no via is required within the dielectric. Since the referenced power plane is no longer continuous, justification was made in the paper to prove that the signal quality was not degraded. Based on the study of imperfect ground plane [16], the dominant factor that influences the EMI property is the return current path: one can either place bypass capacitors or relocate the signal trace to avoid the discontinuity. In this case, Wu et al. suggested an L-bridge pattern that significantly increases the effective inductance by having the spiral arms extended from the cell that are much longer than the traditional straight bridges (see Figure 2.4). By adjusting the width of the arms, one can enhance the mutual (bypass) capacitance in-between adjacent cells as well. In addition, it is noted by other researchers that the arms do not have to be a single strip line. For example, π-bridges [17], square metal patches [18] and meandered arms [19] all demonstrated broadening of the stop-band. HFSS simulation and passive measurement are in good agreement and both showed excellent GBN elimination with an average of 60 dB noise suppression. Moreover, measurement for signal quality was also carried out in the time domain with both single-ended and differential signals [20]. It is shown in Figure 2.5 that with 2.5 GHz non-return to zero (NRZ) pseudo-random bit sequence (PRBS) injection, the differential signaling approach has a much more open eye than the single-ended one.

7
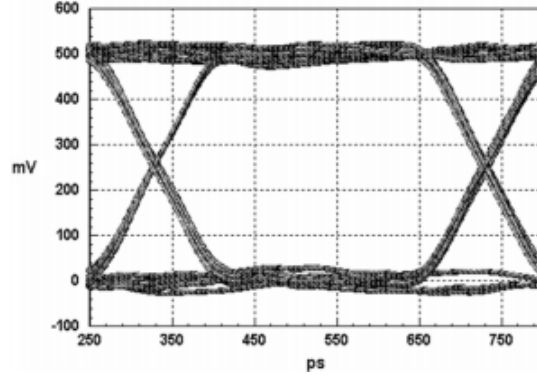
(a) Reference board of continuous power plane
with single-end trace.
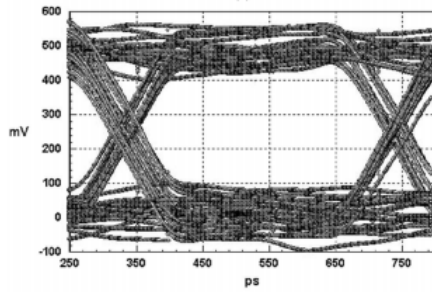
(b) 9-cell LPC-EBG board with
single-end trace.

(c) 9-cell LPC-EBG board with
differential traces.

Figure 2.5: Simulated eye patterns of a patterned EBG power plane [20].

It is worth mentioning that besides qualitative research of the trends of the pattern, numerical analysis and unified circuit model are also available for this type of EBG structure. To obtain a mathematically accurate model, Kim and Schutt-Ainé [21] developed a 2-D circuit-level model of the hybrid planar-type which includes the parameters that were previously ignored in the articles above. The parasitic series capacitance and inductance of the bridge were included in the calculation for the dispersion diagram, yielding results that better correlate with the measurement.

2.3.3 Patterned Array Pair

To further remove the defect from the imperfect reference plane, Kwon et al. suggested a novel array structure (Figure 2.6) that purposely locates EBG unit cells on both power and ground plane to remove SSN [22]. Originating

from the theory that the return current always flows along the least resistant path, it is reasonable to arrange the patterned plane only around the noise sources and keep most of the reference plane continuous. Since the number of cells relates largely to suppression level but not so much for the suppression band, a trade-off between the cell occupation percentage and the level of noise suppression was made. It is proven in the article that for a known board that has a specific area of critical noise, the ratio of occupation could reduce by half while maintaining a good stop-band from 300 MHz to 5 GHz. A similar observation was obtained by using a different patterned unit cell: in [23], the power and ground plane pair is partially covered by a meandered line (Figure 2.7), resulting in a stop-band from 200 MHz to 20 GHz (Figure 2.8). Under the assumption that the SSN source is known and compact, this method is very attractive for ultra-wideband application.
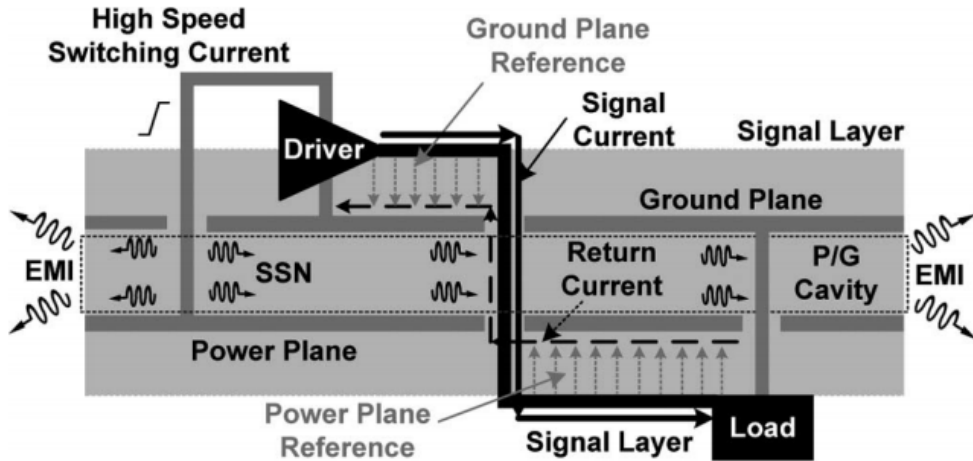
Figure 2.6: Generation and propagation mechanism of SSN in a high-speed multilayer package and PCB structure [22].

2.3.4   Localized Power Island

The power island is the most cost-effective EBG structure among the four categories. Kang et al. take the concept of localization further in that only the via pad is patterned on the power and ground planes [24]. Instead of a square unit cell, a spiral resonator as shown in Figure 2.9 is preferred for
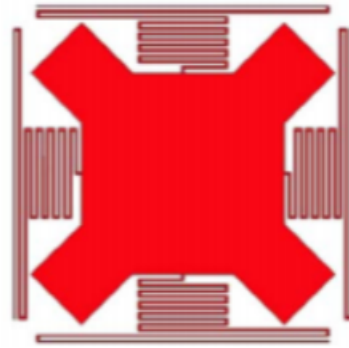
(a) Unit cell pattern.
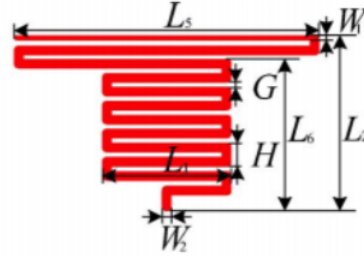
(b) Cell extended meandered arms.
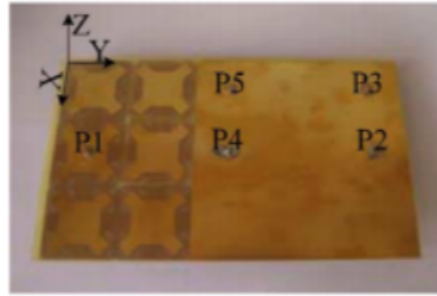
(c) Overview of power plane.
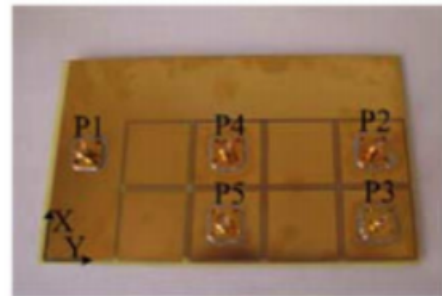
(d) Overview of ground plane.

Figure 2.7: Schematics of the super-localized array design [23].
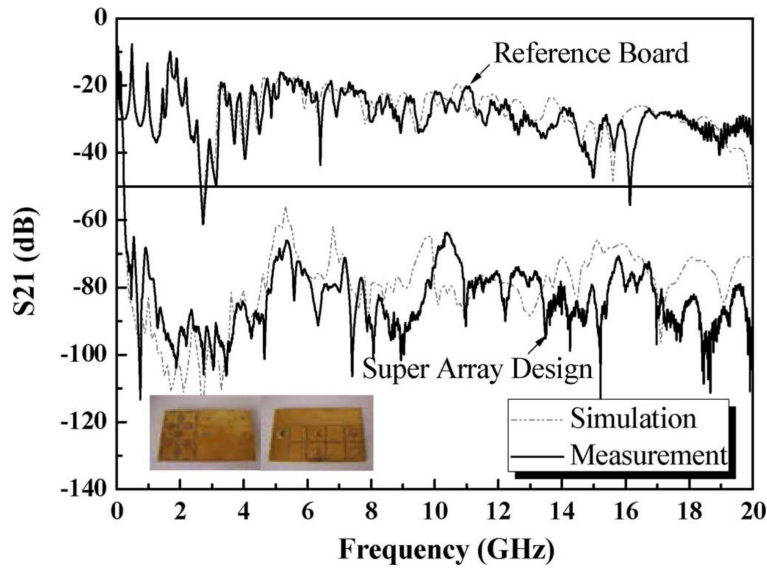
Figure 2.8: Comparison of $|s_{21}|$ obtained by simulation and measurement for the super-localized array design [23].

its compact geometry and inductive nature. Due to the electrically longer current path formed by the structure, its resonant frequency is below 1 GHz with ultra-wideband SSN suppression. Frequency domain simulation and measurement were carried out to show a function stop-band of 200 MHz to 12.5 GHz. As for SI performance, the spiral structure provided an antiparallel current flow, which effectively reduced the generated interference field. The eye diagram from thier measurement shows a dramatic improvement of SI compared to the conventional co-planar EBG structure at 3.33 GHz (6.66 Gb/s). Besides using the circular spiral geometry, Kim and Kim [25] applied a hexagonal spiral (Figure 2.10) which has the same long inductive current path. As expected, the EBG island shows no significant noise peak from 100 MHz to 6 GHz.
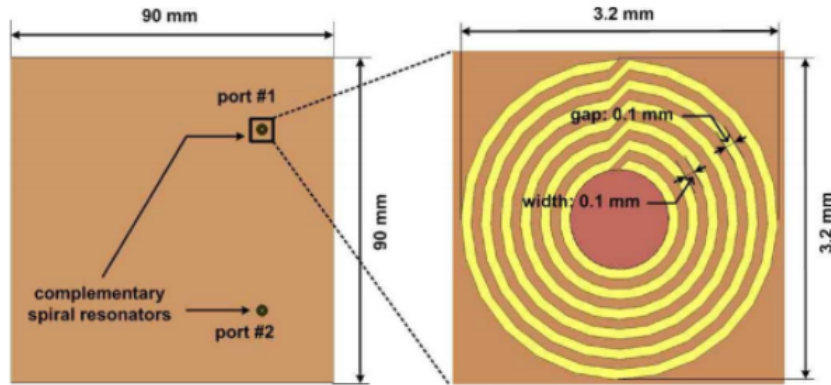
Figure 2.9: Configuration and dimensions of the spiral resonator [24].
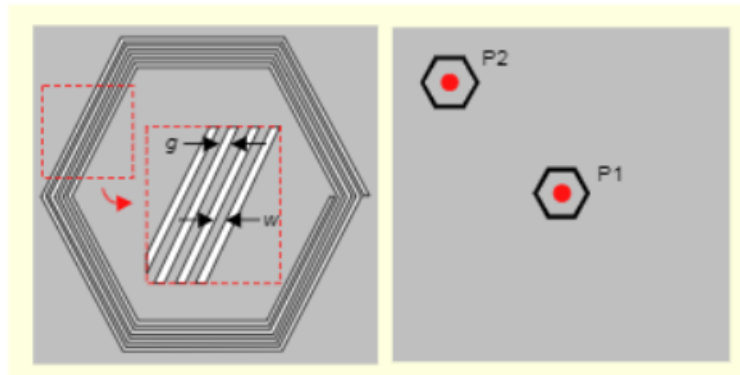
Figure 2.10: Hexagonal spiral pattern on power plane [25].

CHAPTER 3

EQUIVALENT CIRCUIT FORMULATION

As stated in Chapter 2, the design methodology of EBG in PDN application is quite simple and straightforward: Overlapping the forbidden band of EBG with the SSN noise band. Just like many RF and microwave circuit designs, the process flow is recursive rather than a one-time effort. Besides the device's physical specifications, consideration of the following items must take place in a timely fashion at each step to ensure the process is dependable:

1. Resonance frequency needs to be in the center of the SSN noise band.

2. Bandwidth needs to cover suppression from DC to clock frequency.

3. SI degradation due to imperfect reference plane needs to be minimized.

3.1   RF and Microwave Filter Design Theory

Given that the SSN and GBN are known to be in a certain frequency band, the first step of the design is to determine the resonant frequency of a unit EBG cell. The rule of thumb is to take the middle point between the low cutoff frequency (f_L) and high cutoff frequency (f_H). Although it is ideal to have a high-pass filter where all noise from DC to clock frequency is covered, the absolute DC coverage is usually impractical due to feature size constraint. Therefore, some trade-off must be decided, leaving the partial noise band to be resolved by the embedded capacitors on the signal layers. The next step is to choose appropriate inductance (L) and capacitance (C) of the band-pass filter. For a sinusoidal steady-state excitation, resonance frequency (ω_0) is related to L and C in parallel by

$$\omega_0 = \frac{1}{\sqrt{LC}} \tag{3.1}$$

and the filter's quality factor (Q_p), 3 dB bandwidth ($\Delta\omega$) and impedance ($Z(j\omega)$) are given by Equations (3.2), (3.3) and (3.4) respectively.

$$Q_P = \frac{R_P}{\omega_0 L} = \sqrt{\frac{C}{L}} R_P \tag{3.2}$$

$$\Delta\omega = \frac{\omega_0}{Q_P} \tag{3.3}$$

$$Z(j\omega) = \frac{R_P}{1 + jQ_P\left(\frac{\omega}{\omega_0} - \frac{\omega_0}{\omega}\right)} \tag{3.4}$$

To complete the unit cell calculation, the relation between the LC values and EBG geometry is illustrated in Figure 3.1. The capacitance is introduced by the gap between the power and ground planes as well as the distance between the periodic patterns. The inductance comes from the current flowing along the top and bottom conducting layers. If an extra decoupling capacitor (decap) is used in the system, its reactance can be included in the model by adding another pair of LC on top of the existing model. The effect of the decap's finite lead inductance at high frequency is illustrated in Figure 3.2, where both $L_{parasitic}$ and C values contribute to the circuit's impedance by $Z_{decap} = j\left(-\frac{1}{\omega C} + \omega L_{parasitic}\right)$. Therefore, it is possible to construct an equivalent circuit model based on the dimensions and configuration of any EBG structure.
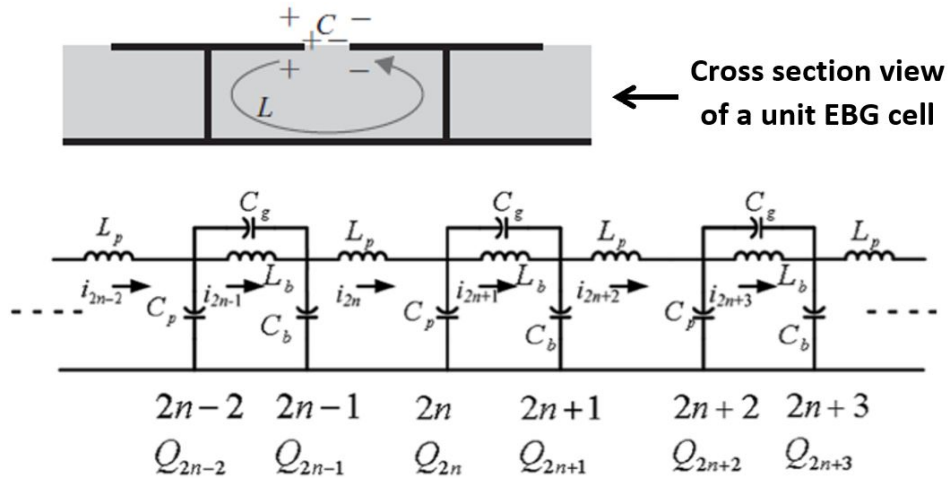
Figure 3.1: Relation between EBG geometry and its equivalent circuit representation for the connecting unit cells.
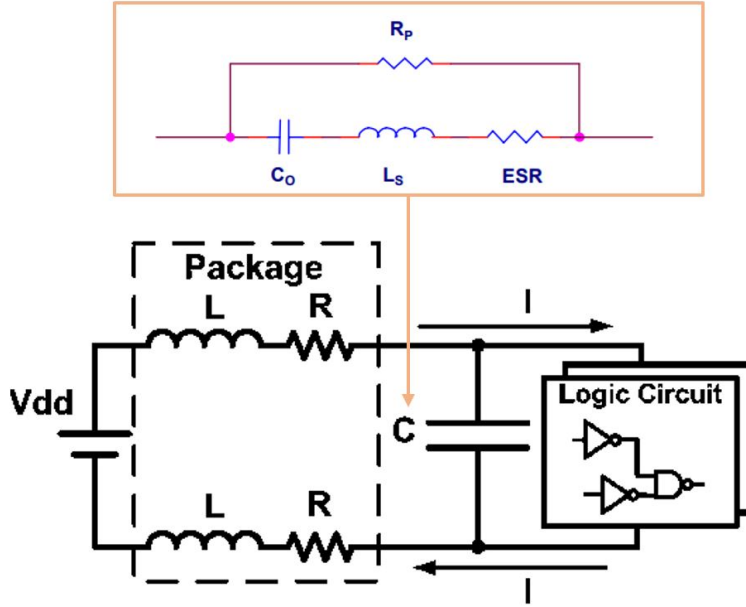
Figure 3.2: Decoupling capacitor's equivalent circuit model with finite lead inductance at high frequency (approximately ≥ 600 MHz).

3.2 Sample Structure Analysis

In this section, two example analyses are presented to demonstrate the effectiveness of the equivalent circuit construction method mentioned above. The calculated results are then compared to the numerical values from the literature for validation.

3.2.1 Example on U-bridge Design

Given the EBG structure in Figure 3.3, it can be seen that L_e and C_e are parameters within the unit cell while L_u and C_u are parameters introduced by the gap between the cells. On further inspection, it is natural to conclude that C_e is a function of area of the square patch (S), substrate height (h) and permittivity (ϵ) based on the basic capacitance formulation. The calculation for L_e follows the same trend of using the basic inductance formula, which is expressed as a function of arm length (len), arm width (w), substrate height
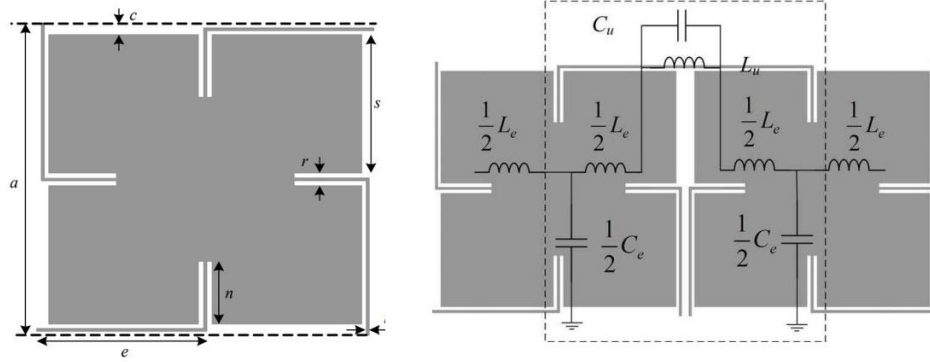
Figure 3.3: Equivalent circuit model for one unit of the U-bridged coplanar EBG structure [27].

(h) and permeability (μ). C_u and L_u can be found in [26] where p is the center-to-center distance between the cells, g is the gap distance and l is the total side length of the unit cell. The formulations are summarized below.

$$
\begin{aligned}
C_e &= \varepsilon_0 \varepsilon_r \frac{S}{h} \\
L_e &= \mu_0 h \frac{len}{w} \\
C_u &= \frac{\varepsilon_0 \left(1 + \varepsilon_r\right) l}{\pi} \, cosh^{-1}\left(\frac{p}{g}\right) \\
L_u &= len \cdot k \cdot ln(2\pi h/w), \quad k = 0.2 \, \mathrm{nH/mm}
\end{aligned}
\tag{3.5}
$$

After substituting in the design dimensions in [27], three parameters in Equation set (3.5) are evaluated to be $C_e = 20.03$ pF, $L_e = 30.5$ nH and $L_u = 75.86$ nH. Note that C_u is extremely small for typical PCB structures and so can be omitted from cut-off frequency calculation. Finally, applying Equation (3.1) up to the model frequency gives

$$
\begin{aligned}
f_L &= \frac{1}{\pi}\sqrt{\frac{1}{(L_e + L_u) \cdot C_e}} = 218.2 \, \mathrm{MHz} \\
f_H &= f_{1,0} = \frac{1}{2l\sqrt{\mu\varepsilon}} = 5 \, \mathrm{GHz}
\end{aligned}
\tag{3.6}
$$
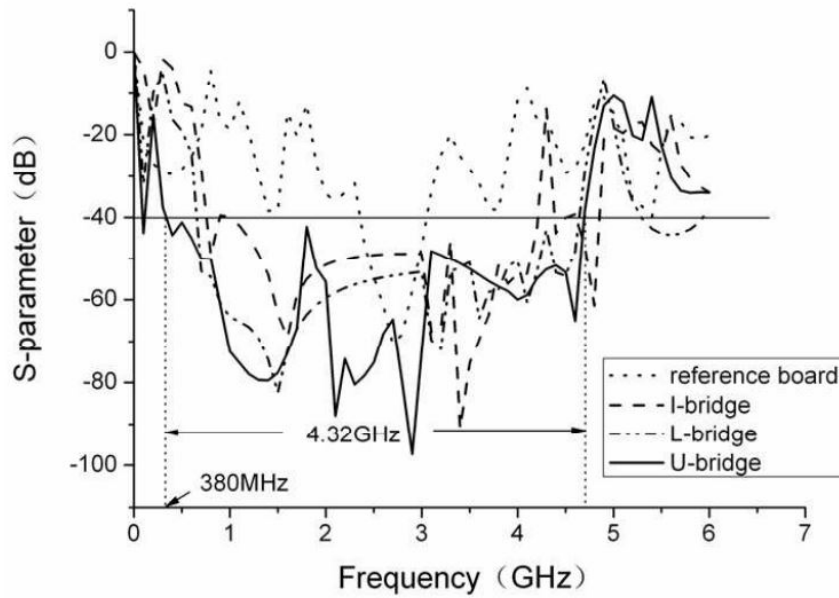
Figure 3.4: $|S_{21}|$ of the U-bridged EBG board by the HFSS simulation. Stop-band starts at 380 MHz and ends at 4.32 GHz [27].

The numerical result for the same structure obtained by HFSS is shown by the solid line in Figure 3.4. Comparing it with the analytic results above, there is around 20% error with the actual stop-band being narrower.

3.2.2 Example on Low-period Design

Using the same approach as in the previous example, the low-period design in Figure 3.5 can be simplified to the circuit schematic shown in Figure 3.1. The design parameters are given in Table 3.1 and the calculation is carried out in Equation set (3.7).

Table 3.1: Design parameters for the low-period coplanar EBG.

Parameters	Value	Parameters	Value
Metal line width w	1 mm	Dielectric thickness h	0.4 mm
Unit cell period d	30 mm	Bridge length l	5 mm
Half-gap width p_1	1 mm	Patch gap width p_2	1 mm
Relative permittivity ϵ_r	4.3	Inductance constant k	0.2 nH/mm
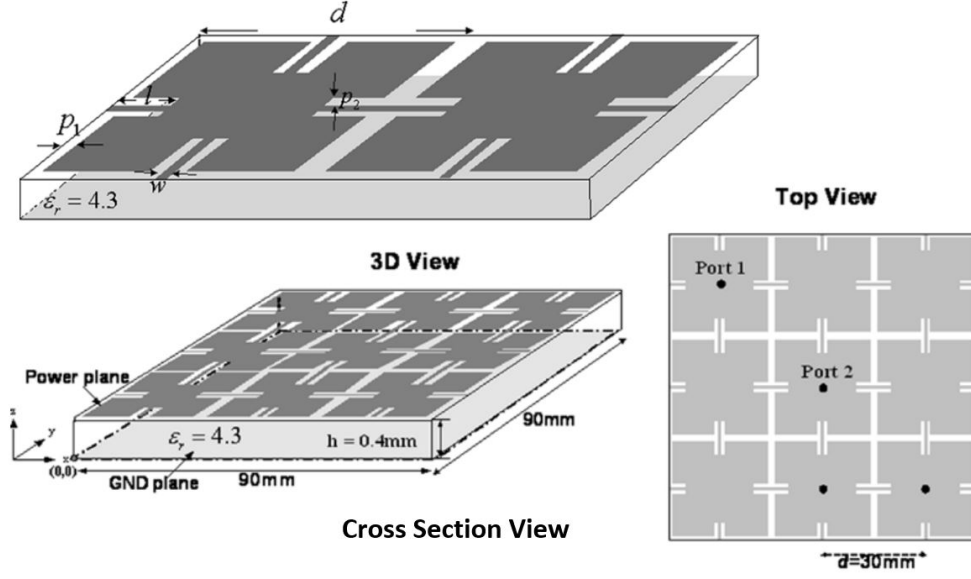
Figure 3.5: Schematic of low-period coplanar 9-cell EBG board [20].

$$C_P = \varepsilon_r \varepsilon_0 \frac{(d - 2l)^2}{h} = 38.055 \text{ pF}$$

$$C_g = (d - 2p_2 - w) \frac{\varepsilon_0 (1 + \varepsilon_r)}{\pi} \cdot cosh^{-1} \left(\frac{d}{2p_1} \right) = 1.37 \text{ pF}$$

$$C_b = (d - 2p_2 - w) \frac{\varepsilon_0 (1 + \varepsilon_r)}{\pi} \cdot cosh^{-1} \left(\frac{d}{2p_2} \right) = 1.37 \text{ pF} \qquad (3.7)$$

$$L_P = \mu_0 \cdot h = 0.503 \text{ nH}$$

$$L_b = k \cdot ln \left(\frac{2\pi h}{w} \right) = 1.84 \text{ nH}$$

From the LC values above, the predicted stop-band is

$$f_L = \frac{1}{\pi} \sqrt{\frac{1}{(L_p + L_b) \cdot (C_g + C_b + C_p)}} = 1.03 \text{ GHz}$$

$$f_H = \frac{1}{(d - 2p_2 - w)\sqrt{\mu_0 \varepsilon_r \varepsilon_0}} = 5.35 \text{ GHz} \qquad (3.8)$$

which has bandwidth of 4.32 GHz. Compared to the measured board that has the stop-band (shown in Figures 3.6 and 3.7) of 4.1 GHz, the error margin is again 20% due to cell repetition and dielectric loss.

Figure 3.6: $|s_{21}|$ obtained by 3-D-FDTD for 9-cell EBG board [20].

Figure 3.7: $|s_{ij}|$ obtained by vector network analyzer measurement for the noise excited at different locations [20].

CHAPTER 4

MODELING EBG STRUCTURES IN PDN

For complicated structures like PDN, it is best to treat the analytical solutions from Chapter 3 as a design guideline only. Although the intention is to obtain a globally precise equivalent circuit model, it is practically impossible to accommodate all parameters of the system in the formulation. Especially for modern-da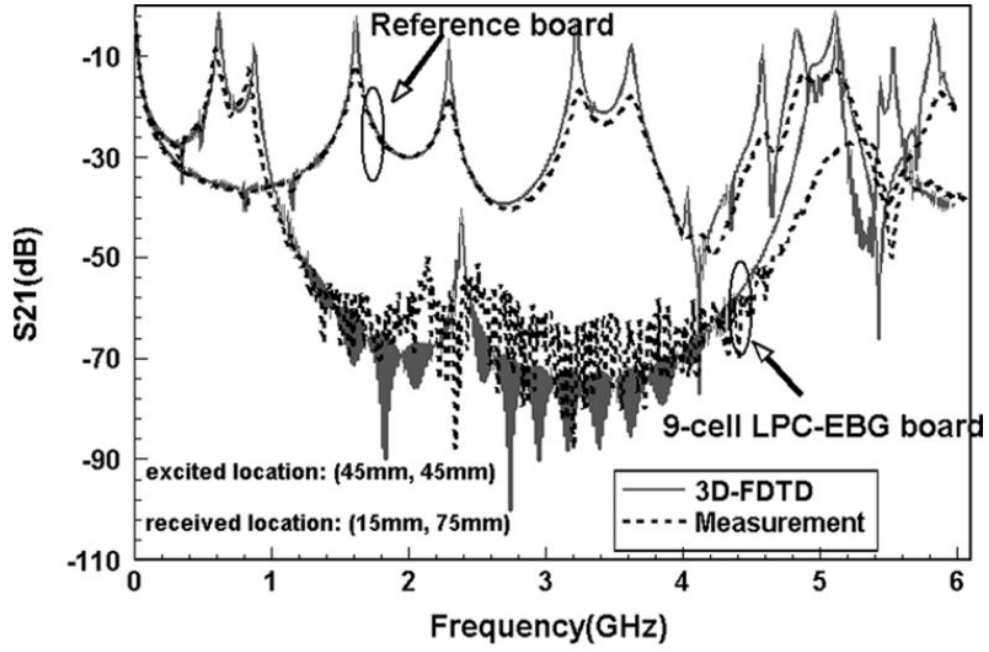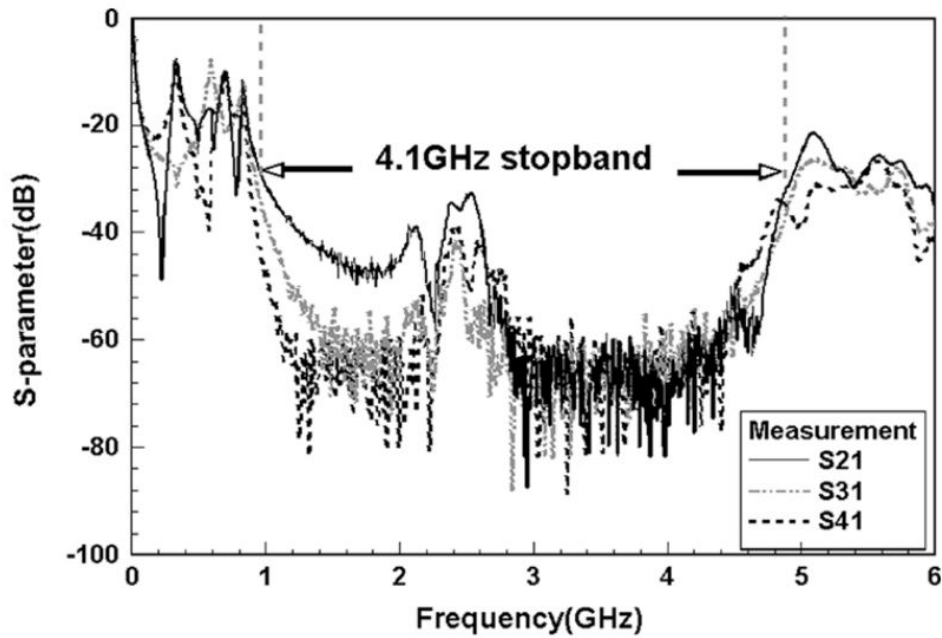y electronics where different modules on the packages are versatile and interchangeable, it is insufficient to develop a grand circuit model for EBG planes without considering the board's packaging, signal layers and numerous vias. In order to effectively verify the performance of EBG structure in various systems, computational electromagnetics is introduced to finalize the design as well as optimize the plane geometry based on the specific application.

4.1 Finite Element Method

The finite element method (FEM) is a commonly used numerical technique that approximates solution of Maxwell's partial differential equations (PDEs) with sets of linear algebraic equations. Compared to the finite difference method in time domain, the major advantage of FEM is its utilization of fine geometry mesh to discretize non-standard shaped objects. For example, Figure 4.1 shows a coarse mesh for a three-unit-cell EBG structure from a commercial FEM solver HFSS. Instead of using the rectangular grid which is commonly found in the finite difference method, FEM allows the usage of affine transformation that maps the arbitrary finite element in $\xi\eta$-plane onto the standardized triangle element in xy-plane (as shown in Figure 4.2) [28]. For this particular case, a tetrahedral element is preferred over triangular because of its extra degree of freedom for 3-D domain. A simple derivation is made below to illustrate how the transformation is done.
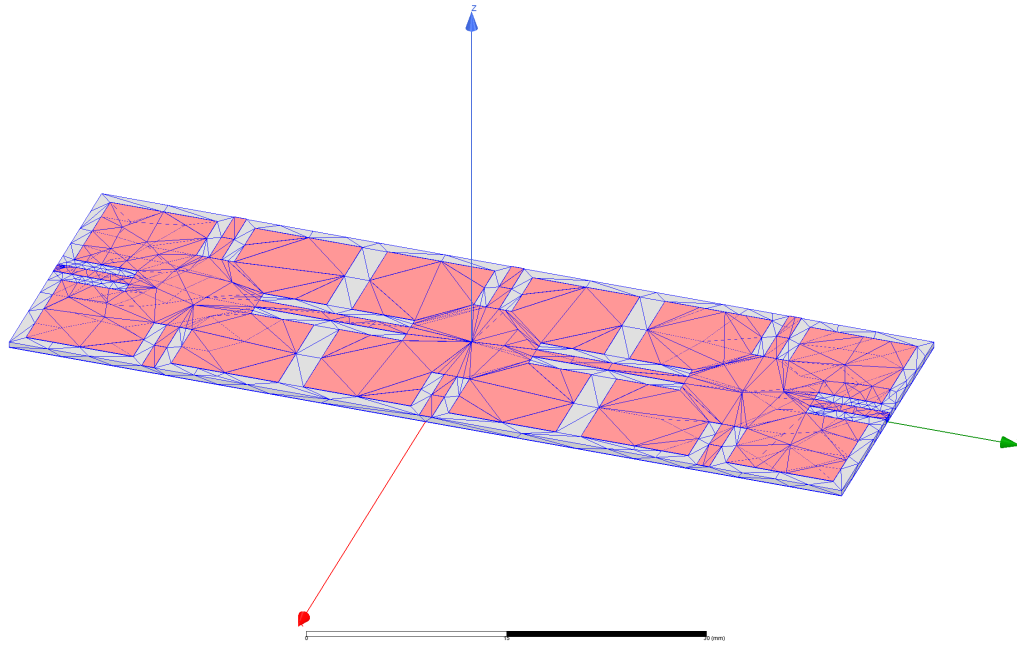
Figure 4.1: Meshing example of a three-unit-cell EBG pattern with two excitation ports in commercial FEM solver HFSS.
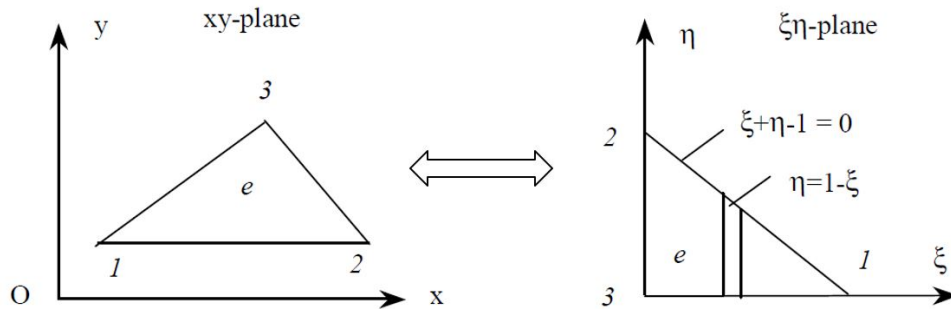

Figure 4.2: Affine transformation that links the standardized triangle in xy-plane with the arbitrary finite element in $\xi\eta$-plane.

The potential ϕ in a tetrahedral element can be approximated as

$$\phi^e(x,y,z) = \sum_{l=1}^{4} \left(\alpha_l + \beta_l x + \gamma_l y + \delta_l z\right)\phi_l^e = \sum_{i=1}^{4} N_l^e \phi_l^e \qquad (4.1)$$

where l denotes each of the vertices of the element e. The terms N_l^e are the scalar interpolating functions that relate to the solution of $\alpha_l, \beta_l, \gamma_l, \delta_l$ by

$$N_l^e(x,y) = \frac{1}{6V^e}\left(\alpha_l^e + \beta_l^e x + \gamma_l^e y + \delta_l^e\right) \qquad (4.2)$$

in which V^e is the volume of the tetrahedral element and

$$J = \begin{vmatrix} 1 & x_1 & y_1 & z_1 \\ 1 & x_2 & y_2 & z_2 \\ 1 & x_3 & y_3 & z_3 \\ 1 & x_4 & y_4 & z_4 \end{vmatrix} = 6V_e \qquad (4.3)$$

$$\alpha_1 = \begin{vmatrix} x_2 & y_2 & z_2 \\ x_3 & y_3 & z_3 \\ x_4 & y_4 & z_4 \end{vmatrix} \quad \alpha_2 = -\begin{vmatrix} x_1 & y_1 & z_1 \\ x_3 & y_3 & z_3 \\ x_4 & y_4 & z_4 \end{vmatrix}$$

$$\alpha_3 = \begin{vmatrix} x_1 & y_1 & z_1 \\ x_2 & y_2 & z_2 \\ x_4 & y_4 & z_4 \end{vmatrix} \quad \alpha_4 = -\begin{vmatrix} x_2 & y_2 & z_2 \\ x_2 & y_2 & z_2 \\ x_3 & y_3 & z_3 \end{vmatrix} \qquad (4.4)$$

$$\beta_1 = -\begin{vmatrix} 1 & y_2 & z_2 \\ 1 & y_3 & z_3 \\ 1 & y_4 & z_4 \end{vmatrix} \quad \beta_2 = \begin{vmatrix} 1 & y_1 & z_1 \\ 1 & y_3 & z_3 \\ 1 & y_4 & z_4 \end{vmatrix}$$

$$\beta_3 = -\begin{vmatrix} 1 & y_1 & z_1 \\ 1 & y_2 & z_2 \\ 1 & y_4 & z_4 \end{vmatrix} \quad \beta_4 = \begin{vmatrix} 1 & y_2 & z_2 \\ 1 & y_2 & z_2 \\ 1 & y_3 & z_3 \end{vmatrix} \qquad (4.5)$$

$$\gamma_1 = \begin{vmatrix} 1 & x_2 & z_2 \\ 1 & x_3 & z_3 \\ 1 & x_4 & z_4 \end{vmatrix} \quad \gamma_2 = -\begin{vmatrix} 1 & x_1 & z_1 \\ 1 & x_3 & z_3 \\ 1 & x_4 & z_4 \end{vmatrix}$$

$$\gamma_3 = \begin{vmatrix} 1 & x_1 & z_1 \\ 1 & x_2 & z_2 \\ 1 & x_4 & z_4 \end{vmatrix} \quad \gamma_4 = -\begin{vmatrix} 1 & x_2 & z_2 \\ 1 & x_2 & z_2 \\ 1 & x_3 & z_3 \end{vmatrix} \qquad (4.6)$$

$$\delta_1 = \begin{vmatrix} 1 & x_2 & y_2 \\ 1 & x_3 & y_3 \\ 1 & x_4 & y_4 \end{vmatrix} \quad \delta_2 = - \begin{vmatrix} 1 & x_1 & y_1 \\ 1 & x_3 & y_3 \\ 1 & x_4 & y_4 \end{vmatrix}$$

$$\delta_3 = \begin{vmatrix} 1 & x_1 & y_1 \\ 1 & x_2 & y_2 \\ 1 & x_4 & y_4 \end{vmatrix} \quad \delta_4 = - \begin{vmatrix} 1 & x_2 & y_2 \\ 1 & x_2 & y_2 \\ 1 & x_3 & y_3 \end{vmatrix}$$

(4.7)

After collecting the terms above, the potential function ϕ can be substituted back to the partial differential equation that defines that boundary condition of the 3-D subject to be solved. Since matrix N is extremely sparse and symmetric, its numerical solution can be easily obtained by many standard solvers. This approach is called the Galerkin method of weighted residuals where differential equations are converted to a discrete problem by weak formulation. The solution can also be carried out analytically after doing integral domain transformation as

$$\iiint_{Ve} (N_1^e)^l (N_2^e)^m (N_3^e)^n (N_4^e)^p \, dV = \frac{l!m!n!p!}{(l+m+n+p+3)!} 6V^e \qquad (4.8)$$

where l, m, n, p are the sizes of the discretized segments.

4.2 Transmission Line Theory

To quantitatively evaluate EBG's noise suppression ability, scattering parameter is introduced for its precision and simplicity. S-parameter describes the electrical properties of a system in a black box fashion, where the wave ratios at selected ports are calculated and arranged into a matrix. An example of a simple two-port network is shown in Figure 4.3. Since s-parameter is designed to characterize high-frequency systems where completely open or
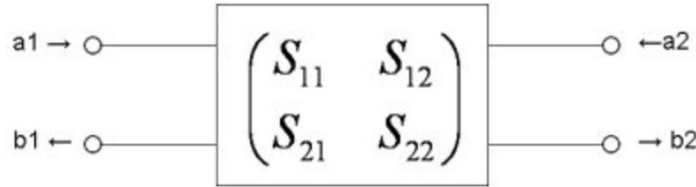

Figure 4.3: General representation of a two-port network.

short circuit does not exit, it is not feasible to express the quantification in terms of voltage and current. Instead, the travelling wave approach is used to separate the forward and backward wave at a given reference plane by

$$v(t) = \mathbf{V}(d)e^{j\omega t} = \underbrace{Ae^{\alpha d}e^{j(\omega t + \beta d)}}_{\text{forward-travelling wave}} + \underbrace{Be^{-\alpha d}e^{j(\omega t - \beta d)}}_{\text{backward-travelling wave}} = V^+ + V^-$$

(4.9)

$$i(t) = \mathbf{I}(d)e^{j\omega t} = \underbrace{\frac{A}{Z_0}e^{\alpha d}e^{j(\omega t + \beta d)}}_{\text{forward-travelling wave}} - \underbrace{\frac{B}{Z_0}e^{-\alpha d}e^{j(\omega t - \beta d)}}_{\text{backward-travelling wave}} = I^+ - I^-$$

(4.10)

where both equations satisfy the second derivative of telegrapher's Equations (4.11) and (4.12) in the form of $y(x) = Ae^{\gamma x} + Be^{-\gamma x}$ with $\gamma = \alpha + j\beta$.

$$\frac{\partial^2 \mathbf{V}(x)}{\partial^2 x} = (R + j\omega L)\frac{\partial \mathbf{I}(x)}{\partial x}$$

(4.11)

$$\frac{\partial^2 \mathbf{I}(x)}{\partial^2 x} = (G + j\omega C)\frac{\partial \mathbf{V}(x)}{\partial x}$$

(4.12)

After normalizing the terms (V^+, V^-, I^+, I^-) with characteristic impedance Z_0, the travelling waves can be defined by

$$a(t) = \frac{V^+(t)}{\sqrt{Z_0}} \qquad b(t) = \frac{V^-(t)}{\sqrt{Z_0}}$$

(4.13)

and from these equations, the s-parameters are summarized as:

$$\begin{aligned} S_{11}(t) &= \left.\frac{b_1(t)}{a_1(t)}\right|_{a_2=0} & S_{21}(t) &= \left.\frac{b_2(t)}{a_1(t)}\right|_{a_2=0} \\ S_{22}(t) &= \left.\frac{b_2(t)}{a_2(t)}\right|_{a_1=0} & S_{12}(t) &= \left.\frac{b_1(t)}{a_2(t)}\right|_{a_1=0} \end{aligned}$$

(4.14)

Note that for s_{ij} representation, port i is where the response is measured and port j is where the signal is injected. Thus s_{21} is refereed as the forward voltage gain (insertion loss) and s_{11} is the input port voltage reflection (return loss). For a passive system, the s-parameter matrix has favorable properties of symmetry and reciprocity, which means $s_{11} = s_{22}$ and $s_{21} = s_{12}$. The matrix can also be applied to multi-port systems as long as Z_0 is consistent.

4.3   Problem Statement

Following the design methodology of patterned power plane and the equivalent filter construction mentioned in the previous chapters, the parameters used in the low-period EBG structure in [20] are further optimized to suppress noise over a wider frequency range. Under practical fabrication conditions, Table 4.1 lists the optimization range for all the design parameters that could contribute to the stop-band. Applying Equations (3.7) and (3.8), these parameters are evaluated with an iterative algorithm to yield a solution set that maximizes the suppression bandwidth within 500 MHz to 10 GHz. The optimized results are also listed in the table with a predicted filter range from 800 MHz to 9.97 GHz. If a 20% error margin is included, the predicted SSN suppression would have a bandwidth of 7.33 GHz.

Table 4.1: Optimization range for the EBG design parameters.

Parameters	Value Range	Optimized Value
Metal line width w	0.5 mm to 5 mm	1.5 mm
Unit cell period d	10 mm to 50 mm	17 mm
Bridge length l	1 mm to 10 mm	6 mm
Half-gap width p_1	0.5 mm to 5mm	0.5 mm
Patch gap width p_2	0.5 mm to 5mm	0.5 mm

The optimization code is shown as Listing 1 at the end of this chapter.

4.4   Environmental Setup

Since the designed EBG structure will be simulated in the commercial FEM solver Ansys HFSS, numbers of project-specific parameters need to be properly adjusted prior to the simulation. For the users who have graduate-level electromagnetic knowledge but have never used this software, the following content provides a detailed explanation how to select the appropriate setup which corresponds to the predefined EM problem.

One of the first decisions to make is the solution type of the model. There are three choices from the menu and each serves a different purpose. "Driven Modal" calculates s-parameter matrix based on the modal and its solution

is expressed in terms of the incident and reflected power of the waveguides'
modes. Oftentimes, if the excitation source is caused by microstrip, trans-
mission line or PPW where a non-TEM mode is supported, this solution
type is preferred because a clear definition of voltage and current at ports is
complicated or even inaccessible. On the other hand, "Driven Terminal" as-
sumes TEM propagation and its solution is expressed in s-parameter matrix
based on the reflective and incident voltage or current at the terminals. An
integration line of E and H field must be defined at each excitation port to
ensure the reference conductor is universal across the board. The last solu-
tion type "Eigenmod" is used when there is no excitation port present. Only
the stored energy in the structure is used for the calculation of its resonant
frequency and its corresponding field.

Next, to ensure versatility of the model, it is strongly suggested that all
design parameters are set as variables rather than constants. This step is
sometimes neglected if the model is directly imported from CAD softwares
like Altium or Cadence. However, given that all parameters in this thesis are
originally drawn in HFSS, it is required to have no set number in the model
so the optimization function can be applied with no further configuration
change. The geometries can be constructed by adding and subtracting var-
ious sizes of polyhedrons. The finished model is shown in Figure 4.4. Note
that the solids are colored based on their corresponding material assignment,
where the connecting edges are actively merged to ensure continuity.

After all the 3-D components are assigned, boundaries of the simula-
tion space must be truncated as the FEM solver needs a finite computa-
tional domain. The default radiation boundary enables the user to create
a truncated air box where the waves impinging onto the surface are ab-
sorbed. This is also called the Sommerfeld radiation condition, which follows
$\hat{n} \times (\nabla \times E) \approx -jk\hat{n} \times (\hat{n} \times E)$ where $\hat{n}$ is the normal unit vector of the
absorbing surface. It is recommend that the boundaries of the air box are
drawn at least $\lambda/4$ away from the structure to fully attenuate the incom-
ing waves. In other scenarios where a strong radiator is present, perfectly
matched layer (PML) should be used because the radiation surface can be
placed very close ($\approx \lambda/8$) to the tested object, thereby reducing the compu-
tation domain. Since the meshing problem in this section is not electrically
large, the default absorbing boundary condition (ABC) is selected and the
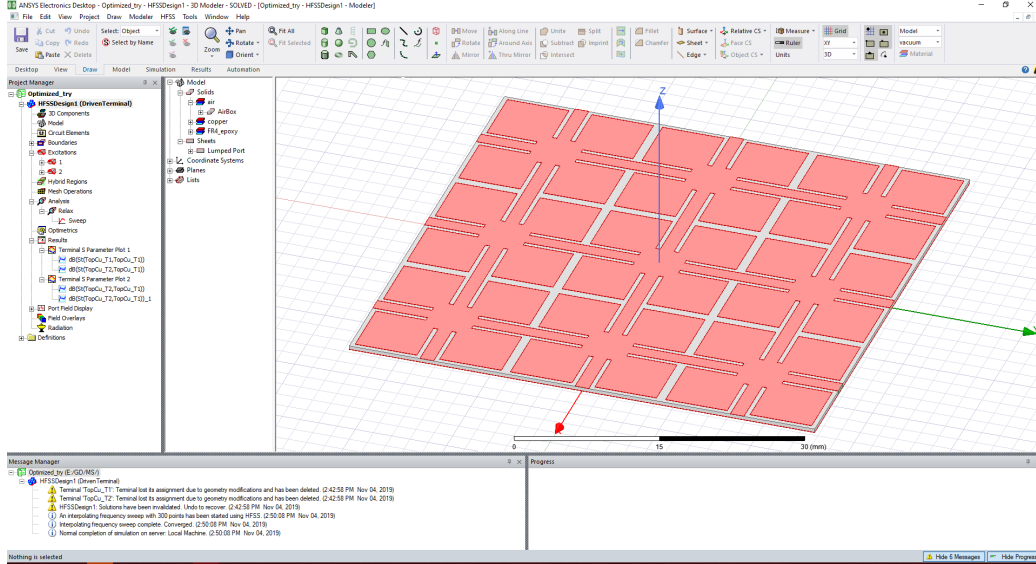truncation space is shown in Figure 4.5 as the semi-transparent blue box.

Figure 4.4: HFSS simulation of low-period EBG structure with the optimized design parameters from Table 4.1.

Given the above environmental setup, the s-parameter matrix of the structure can be obtained by specifying the test ports and simulation range. HFSS provides two types of excitation port and the selection significantly affects the final result. For the case where the geometry is near the port of the excitation, "Lumped Port" is highly preferred for its scalar nature. The excitation associated with this type of port is applied at a sufficiently small area where an equivalent voltage or current is built. Meanwhile, the "Wave Port" is always applied over a cross-section of a structure that is hypothetically connected to a semi-infinitely long waveguide. The test object is assumed to be excited by a quasi-TEM wave located at the external radiation boundary, where the source is a vector field. Therefore, for the EBG structure case, lumped ports are applied at the two end points (as shown in Figure 4.6) because the noise in PDN acts as a small current source that propagates along the vias and then directly flows along the conductor surface. The frequency range of the simulation is set to match the noise band of 100 MHz to 10 GHz with interpolation between the 1000 data points. For fast convergence, maximum delta S (error tolerance) is set to be 0.1 instead of the default 0.02. This completes the setup for the model, and the simulation results are analyzed in the next section.
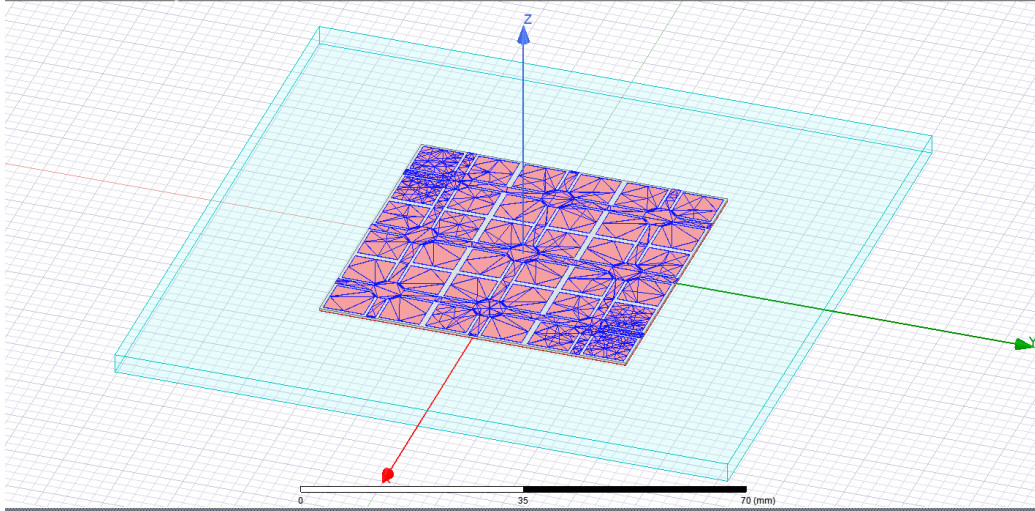
Figure 4.5: Truncated computation domain and meshing grids for the low-period EBG structure in HFSS.
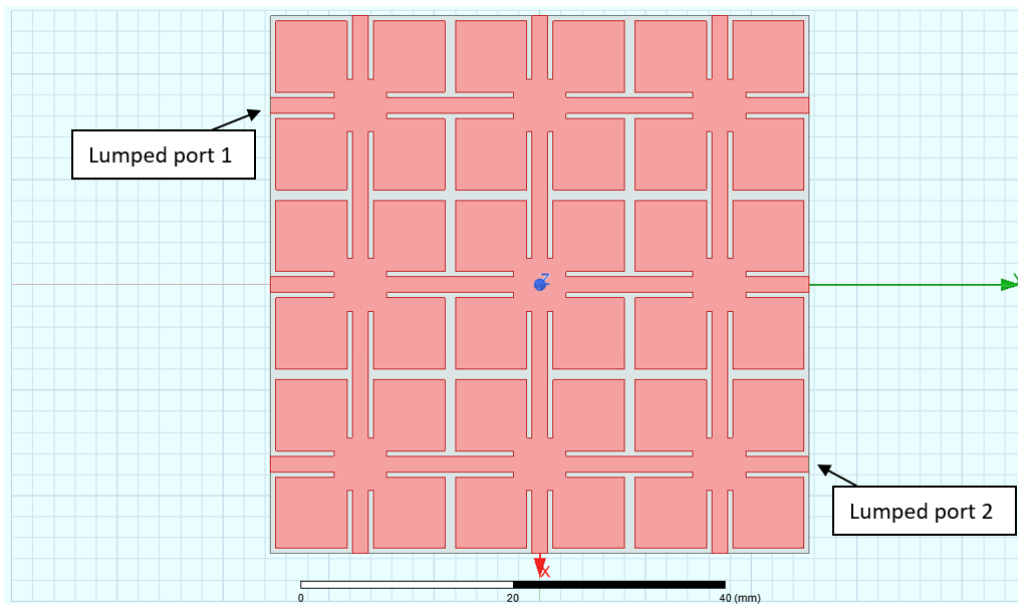

Figure 4.6: Lumped port locations on the simulated structure; both ports' impedances are normalized to 50 Ω.

4.5   Simulation Results and Analysis

The design parameters of the low-period EBG structure from Table 3.1 are simulated in HFSS as the reference board for the optimization. Using the

same ports setup and number of pattern repetitions, the layout for the reference board is shown in Figure 4.7. The corresponding s_{21} matrix is plotted in Figure 4.8, where the filter stop-band lies between 0.97 GHz and 5.05 GHz (assuming a $\leq$ -30 dB cutoff). This simulated bandwidth of 4.08 GHz is very close to the measurement result provided in [20].
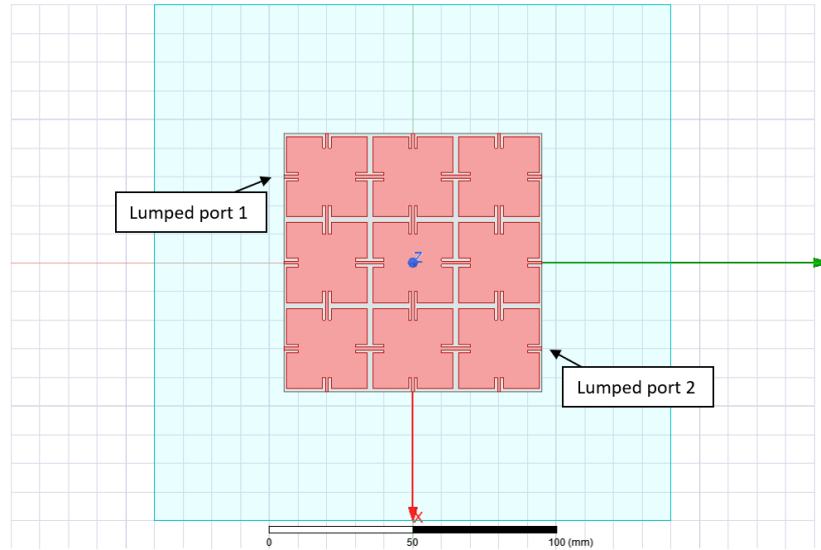

Figure 4.7: Lumped port locations on the reference board.
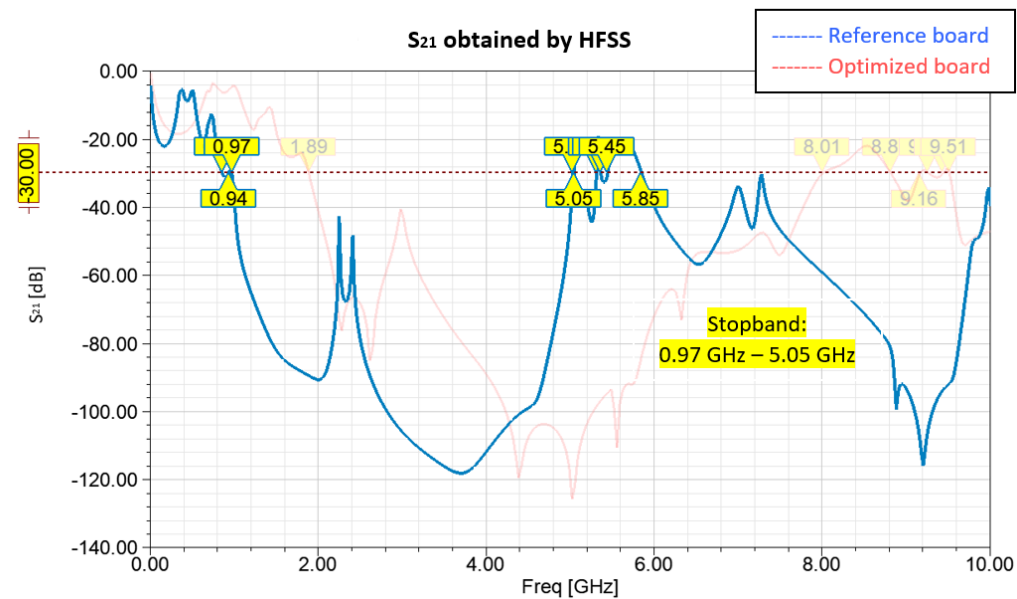
Figure 4.8: s_{21} obtained by HFSS simulation for the reference board.

The HFSS simulation result for the optimized parameters is shown in Figure 4.9. The stop-band extends from 1.89 GHz to 8.01 GHz, giving a bandwidth of 6.12 GHz. Comparing to the reference case of 4.08 GHz, there is a 50% expansion of bandwidth if the optimization parameters are used. Although the analytical prediction did not foresee the lower end of the band to be over 1 GHz, it is always possible to recursively adjust the range of optimization to obtain a better result.
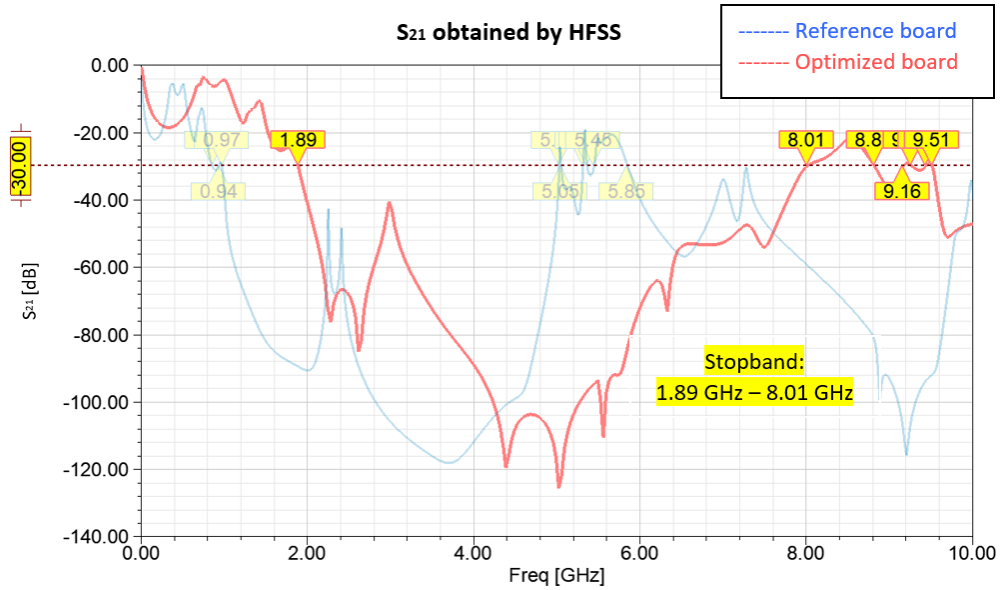
Figure 4.9: s_{21} obtained by HFSS simulation for the optimized board.

```python
1   import numpy as np
2
3   #Setting the constants
4   PI = 3.1415926
5   eps_0 = 8.85e-12
6   eps_r = 4.3
7   miu_0 = 4*PI*1e-7
8   k=0.2e-6
9   h=0.4e-3
10  minf_L = 99999999999999
11  maxf_H = -99999999999999
12  diff = 0
13
14  #Begin optimization with selected range of parameters
15  for D in np.arange(10, 50, 1):
16   for W in np.arange(0.5, 5, 0.5):
17    for P2 in np.arange(0.5, 5, 0.5):
18     for L in np.arange(1,10,1):
19      for P1 in np.arange(0.5, 5, 0.5):
20       w = W*1e-3
21       d = D*1e-3
22       l = L*1e-3
23       p_1 = P1*1e-3
24       p_2 = P2*1e-3
25
26       if (d-2*p_2-w) < 0:
27        continue
28
29       #LC equations from Chapter 3
30       C_p = eps_r*eps_0*( (d - 2*l) *(d - 2*l) ) / h
31       C_g = (d - 2*p_2 - w)*eps_0*(1 + eps_r)/PI*np.arccosh(
          ↪ d/(2*p_1) )
32       C_b = (d - 2*p_2 - w)*eps_0*(1 + eps_r)/PI*np.arccosh(
          ↪ d/(2*p_2) )
33       L_p = miu_0*h
34       L_b = k*np.log(2*PI*h/w)
35
36       f_L = 1/PI*np.sqrt(1/((L_p+L_b)*(C_g+C_b+C_p)))
37       f_H = 1/((d-2*p_2-w)* 6.915296333e-9)
38
39       #SSN bandwidth
40       if f_H*1e-9>10:
41        continue
42       if f_L*1e-9<0.5:
43        continue
44
45       #Print out optimized parameters
46       if f_H - f_L > diff:
47        print(W, D, L, P1, P2, f_L*1e-9, f_H*1e-9)
48        diff = f_H-f_L
```

Listing 1: Python code for optimization of EBG design parameters.

CHAPTER 5

CONCLUSION AND FUTURE WORK

5.1 Conclusion

In this thesis, the complete design flow for EBG pattern is demonstrated and the required background knowledge is provided. With the equivalent circuit formulations and the optimized code illustrated in the previous chapters, an optimized low-period EBG power plane is presented with SSN stop-band 50% wider than that reported in the literature.

5.2 Future Work

In order to fully evaluate the purposed structure's SSN suppression capability, the pattern power plane needs to be tested in a more realistic environment. For instance, a physical board can be fabricated based on the optimized parameters and VNA measurement can be taken to verify the simulation result. Furthermore, the patterned plane can be embedded into an actual PDN inter-connect that has at least two pairs of power/ground layers with multiple vias near the noisy component. In that case, both simulation and measurement can be performance to determine the SI degradation before and after inserting the EBG plane.

REFERENCES

[1] G.-T. Lei, R. W. Techentin, and B. K. Gilbert, "High-frequency characterization of power/ground-plane structures," *IEEE Transactions on Microwave Theory and Techniques*, vol. 47, no. 5, pp. 562–569, May 1999.

[2] R. Abhari, G. V. Eleftheriades, and E. van Deventer-Perkins, "Analysis of differential vias in a multilayer parallel plate environment using a physics-based cad model," *2001 IEEE MTT-S International Microwave Sympsoium Digest*, vol. 3, pp. 2031–2034, May 2001.

[3] A. Madou and L. Martens, "Electrical behavior of decoupling capacitors embedded in multilayered PCBs," *IEEE Transactions on Electromagnetic Compatibility*, vol. 43, no. 4, pp. 549–556, Nov. 2001.

[4] Y. Rahmat-Samii and H. Mosallaei, "Electromagnetic band-gap structures: Classification, characterization, and applications," *2001 Eleventh International Conference on Antennas and Propagation*, vol. 2, pp. 560–564, Apr. 2001.

[5] D. Sievenpiper, L. Zhang, R. F. J. Broas, N. G. Alexopolous, and E. Yablonovitch, "High-impedance electromagnetic surfaces with a forbidden frequency band," *IEEE Transactions on Microwave Theory and Techniques*, vol. 47, no. 11, pp. 2059–2074, Nov. 1999.

[6] E. Yablonovitch, "Inhibited spontaneous emission in solid-state physics and electronics," *Phys. Rev. Lett.*, vol. 58, pp. 2059–2062, 20 May 1987.

[7] D. M. Elsheakh, H. A. Elsadek, and E. A. Abdallah, "Antenna designs with electromagnetic band gap structures," in *Metamaterial*, IntechOpen, 2012.

[8] A. Alù, M. G. Silveirinha, A. Salandrino, and N. Engheta, "Epsilon-near-zero metamaterials and electromagnetic sources: Tailoring the radiation phase pattern," *Phys. Rev. B*, vol. 75, Apr. 2007.

[9] S. Mahmoud, "A new miniaturized annular ring patch resonator partially loaded by a metamaterial ring with negative permeability and permittivity," *Antennas and Wireless Propagation Letters, IEEE*, vol. 3, pp. 19–22, Jan. 2005.

[10] T. Kamgaing and O. M. Ramahi, "High-impedance electromagnetic surfaces for parallel-plate mode suppression in high-speed digital systems," *2002 IEEE 11th Topical Meeting on Electrical Performance of Electronic Packaging*, pp. 279–282, Oct. 2002.

[11] B. Archambeault and A. E. Ruehli, "Analysis of power/ground-plane emi decoupling performance using the partial-element equivalent circuit technique," *IEEE Transactions on Electromagnetic Compatibility*, vol. 43, no. 4, pp. 437–445, Nov. 2001.

[12] R. Abhari and G. V. Eleftheriades, "Metallo-dielectric electromagnetic bandgap structures for suppression and isolation of the parallel-plate noise in high-speed circuits," *IEEE Transactions on Microwave Theory and Techniques*, vol. 51, no. 6, pp. 1629–1639, Jun. 2003.

[13] J. Lee, H. Kim, and J. Kim, "High dielectric constant thin film EBG power/ground network for broad-band suppression of SSN and radiated emissions," *IEEE Microwave and Wireless Components Letters*, vol. 15, no. 8, pp. 505–507, Aug. 2005.

[14] G. Chen, K. Melde, and J. Prince, "The applications of EBG structures in power/ground plane pair SSN suppression," *Electrical Performance of Electronic Packaging*, pp. 207–210, Oct. 2004.

[15] T.-L. Wu, C.-C. Wang, Y.-H. Lin, T.-K. Wang, and G. Chang, "A novel power plane with super-wideband elimination of ground bounce noise on high speed circuits," *IEEE Microwave and Wireless Components Letters*, vol. 15, no. 3, pp. 174–176, Mar. 2005.

[16] Y.-H. Lin and T.-L. Wu, "Investigation of signal quality and radiated emission of microstrip line on imperfect ground plane: FDTD analysis and measurement," *2001 IEEE EMC International Symposium*, vol. 1, pp. 319–324, Aug. 2001.

[17] X.-H. Wang, B.-Z. Wang, Y.-H. Bi, and W. Shao, "A novel uniplanar compact photonic bandgap power plane with ultra-broadband suppression of ground bounce noise," *IEEE Microwave and Wireless Components Letters*, vol. 16, no. 5, pp. 267–268, May 2006.

[18] J. Choi, V. Govind, M. Swaminathan, and K. Bharath, "Noise isolation in mixed-signal systems using alternating impedance electromagnetic bandgap (AI-EBG) structure-based power distribution network (PDN)," *IEEE Transactions on Advanced Packaging*, vol. 33, no. 1, pp. 2–12, Feb. 2010.

[19] J. Qin and O. M. Ramahi, "Ultra-wideband mitigation of simultaneous switching noise using novel planar electromagnetic bandgap structures," *IEEE Microwave and Wireless Components Letters*, vol. 16, no. 9, pp. 487–489, Sep. 2006.

[20] T.-L. Wu, Y.-H. Lin, T.-K. Wang, C.-C. Wang, and S.-T. Chen, "Electromagnetic bandgap power/ground planes for wideband suppression of ground bounce noise and radiated emission in high-speed circuits," *IEEE Transactions on Microwave Theory and Techniques*, vol. 53, no. 9, pp. 2935–2942, Sep. 2005.

[21] K. H. Kim and J. E. Schutt-Ainé, "Analysis and modeling of hybrid planar-type electromagnetic-bandgap structures and feasibility study on power distribution network applications," *IEEE Transactions on Microwave Theory and Techniques*, vol. 56, pp. 178–186, Jan. 2008.

[22] J. H. Kwon, D. U. Sim, S. I. Kwak, and J. G. Yook, "Novel electromagnetic bandgap array structure on power distribution network for suppressing simultaneous switching noise and minimizing effects on high-speed signals," *IEEE Transactions on Electromagnetic Compatibility*, vol. 52, no. 2, pp. 365–372, May 2010.

[23] Y. He, C. Liang, and Q. H. Liu, "Novel array EBG structures for ultra-wideband simultaneous switching noise suppression," *IEEE Antennas and Wireless Propagation Letters*, vol. 10, pp. 588–591, 2011.

[24] H. Kang, H. Kim, H. Lee, and J. Yook, "An enhanced power plane topology using localized spiral resonator for wideband suppression of simultaneous switching noise," *2009 IEEE Antennas and Propagation Society International Symposium*, pp. 1–4, Jun. 2009.

[25] B. Kim and D.-W. Kim, "Bandwidth enhancement for SSN suppression using a spiral-shaped power island and a modified EBG structure for a $\lambda/4$ open stub," *ETRI Journal*, vol. 31, no. 2, pp. 201–208, Apr. 2009.

[26] M. Rahman and M. Stuchly, "Transmission line-periodic representation of planar microwave phototic bandgap structures," *Microwave and Optical Technology Letters*, vol. 30, pp. 15–19, Jul. 2001.

[27] X.-J. Wang and L.-F. Shi, "Novel coplanar EBG low pass filter," *Progress In Electromagnetics Research Letters*, vol. 48, pp. 83–93, Jan. 2014.

[28] J. Jin, *Theory and Computation of Electromagnetic Fields*. John Wiley and Sons, 2010.